SINTEF

2020:01299- Unrestricted

Report

Microstructural Characterization and In-Situ Nano/Micromechanical Testing of Hydrogen Pre-charged Pipeline Steels

HyLINE WP2: Nano and micro scale effects

Anette Brocks Hagen
Dong Wang
Pernille Fathi

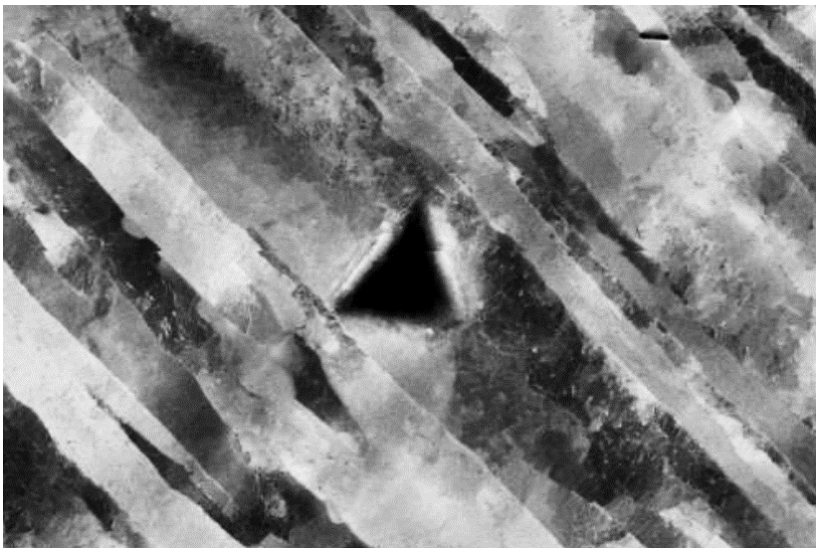

SINTEF Industry
Materials Integrity and Welding
2021-06-17

SINTEF Industri
SINTEF Industry
Address:
Postboks 4760 Torgarden
NO-7465 Trondheim
NORWAY
Switchboard: +47 40005100

info@sintef.no

Enterprise /VAT No:
NO 919 303 808 MVA

KEYWORDS:
In-situ micromechanical tensile testing
Nanoindentation
Pipeline steel
Hydrogen embrittlement

Report

Microstructural Characterization and In-Situ Nano/Micromechanical Testing of Hydrogen Pre-charged Pipeline Steels

VERSION
1.1

DATE
2021-06-17

AUTHOR(S)
Anette Brocks Hagen
Dong Wang
Pernille Fathi

CLIENT(S)
RCN, Gassco, Equinor, TechipFMC, NEL, Air Liquide

CLIENT'S REF.
Andreas Bratland, RCN

PROJECT NO.
102017484-4

NUMBER OF PAGES/APPENDICES:
29

ABSTRACT
The hydrogen susceptibility on mechanical properties of a new (Steel A) and a "vintage" (Steel B) X65 pipeline steel, have been investigated by (1) in-situ micromechanical tensile testing and (2) in-situ electrochemical nanoindentation. The tensile samples were extracted from the inner and middle position in longitudinal and transverse direction of the pipe and tested in-situ in a scanning electron microscope (SEM) under four environmental conditions: after 24 -and 96 hours of hydrogen pre-charging, in vacuum (~10^{-5} Pa) (without pre-charging) and in air outside the SEM chamber, for comparison. Nanoindentations were performed on the different microstructures in both Steel A and Steel B. Fractography and SEM characterization techniques such as electron backscatter diffraction (EBSD) and electron channelling contrast imaging (ECCI) analysis were performed to reveal details in both microstructures and hydrogen-related degradation after mechanical tests.

PREPARED BY
Anette Brocks Hagen

SIGNATURE
Anette Hagen
Anette Hagen (Jun 17, 2021 13:35 GMT+2)

CHECKED BY
Antonio Alvaro

SIGNATURE
Antonio Alvaro (Jun 24, 2021 12:38 GMT+2)

APPROVED BY
Ragnar Fagerberg

SIGNATURE
Ragnar Fagerberg
Ragnar Fagerberg (Jun 24, 2021 12:28 GMT+2)

REPORT NO.	ISBN	CLASSIFICATION	CLASSIFICATION THIS PAGE
2020:01299	978-82-14-06448-3	Unrestricted	Unrestricted

Document history

VERSION	DATE	VERSION DESCRIPTION
Version 1	2020-11-26	
Version 1.1	2021-06-17	The received material certificate for one of the steels in the HyLINE project is not correct. In the current version (1.1), the descriptions related to the incorrect material information from the certificate, have been removed.

Table of contents

1 Introduction

The report summarizes the work related to the small-scale testing and advanced characterisation performed within Work Package 2 (WP2) in the HyLINE project, with the aim to increase the understanding and address local hydrogen-related deformation and degradation mechanisms in a modern -and vintage X65 pipeline steel, both being potential candidates for transporting pressurized gaseous hydrogen. The current work is a part of on-going research and future results will be published in journal papers and following report(s).

A detailed description of the materials and its metallurgical features is provided in *2 Materials and Experimental Methods*. Experimental methods and the characterization techniques utilized are described together with relevant parameters and theory. The main investigation methods used are in-situ tensile testing and nanoindentation; in the latter, the samples are pre-charged before mechanically tested inside the SEM. However, this methodology is currently under development to allow for in-situ hydrogen charging setup.

The following section, *3 Results*, provide an overview of the obtained data from mechanical testing and characterization of hydrogen influence of the microstructural features and address local failures due to the presence of hydrogen, with emphasis on the local mechanical properties.

Finally, *4 Summarizing Remarks* highlights the main findings.

2 Material and Experimental Methods

2.1 Materials

2.1.1 Steel A (new pipeline steel)

One of the investigated materials is an API 5L grade X65 pipeline steel that covers seamless and welded steel line pipe suitable for gas, water and oil transport. This steel grade has a minimal yield strength and tensile strength of 448 MPa (65 KSI) and 531 MPa (77 KSI), respectively. The chemical composition and the carbon equivalent, calculated from Eq. 1, are given in Table 1. The mechanical properties given in the certificate and determined from mechanical tests at SINTEF, are presented in Table 2. The specimens tested at SINTEF, are extracted from three different positions in the pipewall thickness, i.e., from the inner pipewall in longitudinal direction, from the mid-thickness in longitudinal direction and from the mid-thickness in the transversal direction, referred to as T2, T3 and T5.

$$CE = \%C + \frac{\%Mn + \%Si}{6} + \frac{\%Cr + \%Mo + \%V}{5} + \frac{\%Cu + \%Ni}{15} \quad \textbf{Eq. 1}$$

Table 1: Chemical composition of X65 Steel A.

Element	C	Si	Mn	P	S	Cu	Cr	Ni	Mo	V	Nb	Ti	N	Al	CE
Wt. %	0.07	0.23	1.17	0.01	0.002	0.14	0.17	0.15	0.13	0.03	0.02	0.002	0.07	0.031	**0.39**

Table 2: Mechanical properties of X65 Steel A given in certificate and from tensile tests performed at SINTEF. Tests are performed at room temperature with a strain rate of $2.5 \cdot 10^{-4}$ s^{-1}.

	$\sigma_{0.2}$ [MPa]	σ_{UTS} [MPa]	HV
As received	498*	583	-
T2 air	495	576	190 (± 1.8)
T3 air	564	633	203 (± 1.1)
T5 air	543	610	-

***Definition of yield strength is $\sigma_{0.5}$ for the data given in the certificate for Steel A.**

Representative microstructure characteristics of Steel A are shown in the optical micrographs in Figure 1. The base metal consists of ferrite and bainite resulting from quenching and tempering. The bainite is a mixture of dislocation-rich ferrite and cementite. The carbon content is higher than in ferrite, making bainite less ductile, harder and more brittle. Yield strength and tensile strength of steel increases linearly with the carbon concentration [1, 2]. As shown from the mechanical properties in Table 2, the inner pipewall, i.e., T3, features a higher yield strength. This is suggested to originate from the higher volume fraction of bainite, qualitatively seen from SEM imaging, EBSD and optical microscopy. A detailed description of microstructure, including the hardness variations through thickness, is also given in the HyLINE screening report for all the relevant materials in the project [3].

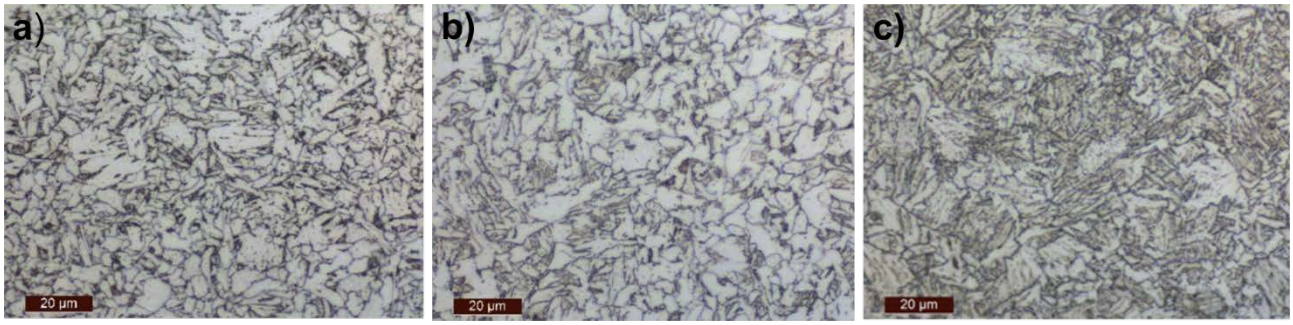

Figure 1: Optical micrographs of Steel A from the a) outer, b) middle and c) inner position of the pipewall thickness. Imaging performed in the transverse direction of the pipe.

2.1.2 Steel B (vintage pipeline steel)

The other investigated material is also an API 5L grade X65 pipeline steel, that covers seamless and welded steel line pipe suitable for gas, water and oil transport. It has a specified minimal yield strength (SMYS) and tensile strength of 448 MPa (65 KSI) and 531 MPa (77 KSI), respectively. The pipeline is produced in 1982 and manufactured with the conventional Thermo-Mechanical Controlled Processing (TMCP) by the Japanese steel manufacturer Fukuyama Steel Works. It is a two-pass submerged Arc welded steel pipe. However, weldments and Heat-Affected zones are not considered in this Report.

Optical micrographs of the Steel B material are shown in Figure 2. The microstructure consists of equiaxed ferritic grains homogeneously distributed in addition to pearlite and (probably) granular bainite. Pearlite/bainite are developed in a banded appearance that can give rise to anisotropy of the mechanical properties [4]. The banding changes its characteristics throughout the thickness and become wider in the centre of the pipe thickness. Also, ferrite grains are coarser in the middle of the pipe wall thickness. Another peculiar microstructural feature of the Steel B material is the granular bainite present within the pearlite bands. The Mn content can contribute to the formation of ferritic bands as well as undesirable bainite bands in zones with higher concentration of Mn. The bainitic bands, referred to as abnormal segregation bands, can reduce the plasticity of the steel and are reported to cause quasi cleavage fractures [5, 6]. The harder and more brittle mechanical properties of the abnormal segregation bands can probably be of relevance for the mechanical properties in hydrogen environment.

The chemical composition and the carbon equivalent, calculated from Eq. 1, are given in Table 3. The mechanical properties given in the certificate and determined from mechanical tests at SINTEF, are given in Table 4. In the similar manner as for Steel A, specimens were extracted from the inner (longitudinal direction), middle (longitudinal direction) and middle (transversal direction) position of the pipewall thickness, schematically illustrated in Figure 3.

Table 3: Chemical composition of X65 Steel B.

Element	C	Si	Mn	P	S	Cu	Cr	Ni	Mo	V	Nb	Ti	N	CE
Wt. %	0.1	0.15	<1.6	<0.025	<0.015	<0.25	<0.25	<0.25	<0.05	<0.1	<0.05	<0.02	0.1	**0.56**

Table 4: Mechanical properties of Steel B steel given in certificate and from tensile tests performed at SINTEF. Tests are performed at room temperature with nominal strain rate of $2.5 \cdot 10^{-4}$ s^{-1}.

	$\sigma_{0.2}$ [MPa]	σ_{UTS} [MPa]	HV
As received	526	627	-
S2 air	445	584	187 (± 0.6)
S3 air	518	590	185 (± 0.2)
S5 air	507	598	-

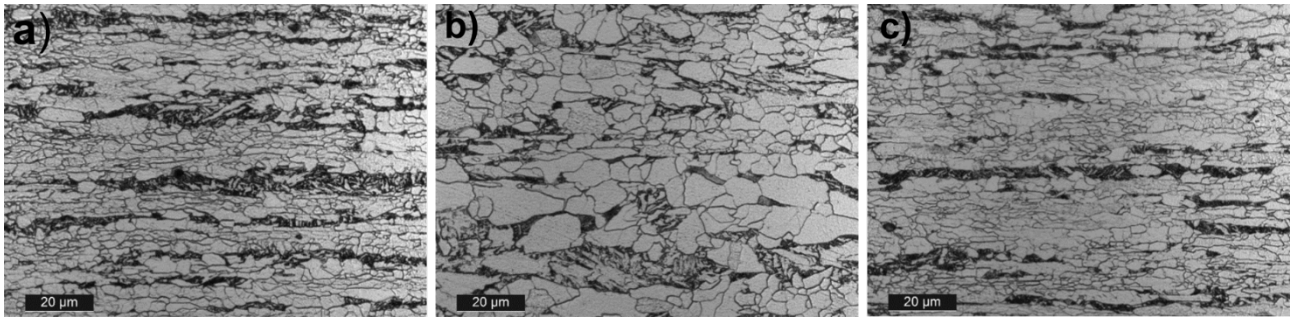

Figure 2: Optical micrographs of Steel B from the a) outer, b) middle and c) inner position of the pipewall thickness. Imaging performed in the transverse direction of the pipe.

2.2 Sample geometry and Preparation

The microstructure of both pipeline steels slightly differs across the pipe wall thickness as shown in Figure 1 and Figure 2, which commonly occurs due inhomogeneous cooling in particular areas of the pipe during the manufacturing procedure and depends on several factors, including the pipewall thickness. For this reason, the outer, middle and inner region of the pipewall was investigated in both longitudinal and transverse direction. Two different geometries of samples were prepared, depending on the test method: dog-bone tensile samples for micromechanical tensile tests and disc shaped 12 mm diameter samples with a thickness of 2 mm for in-situ electrochemical nanoindentation (ECNI). Tensile samples were cut out from both longitudinal and transverse directions in the middle and inner area of the pipe, while discs used for nanoindentation were cut from the middle of the pipewall thickness.

An overview of the test areas is presented in Table 5 and schematically illustrated in Figure 3. The specimen geometry used for micromechanical test in this work, is shown in Figure 3 (b). Twelve tensile specimens from both materials were cut and metallographically prepared. No evidence of significant microstructural differences was observed between samples extracted from similar region. The samples were grinded using SiC papers with grit sizes from 80 to 4000 and polished with 3-µm and 1-µm diamond suspensions. Samples investigated by optical microscopy were etched with 2% Nital solution while the samples prepared to be analysed by EBSD, SEM and nanoindentation tests were treated with oxide polishing suspension (OPS) with 200 nm grain size for 20 min.

Table 5: Material, directions and positions samples tested in this work. Numbered positions are illustrated Figure 3.

Materials	**Steel A**		**Steel B**	
Direction	Longitudinal	Transversal	Longitudinal	Transversal
Position	Middle (2) and inner (3)	Middle (5) and inner (6)	Middle (2) and inner (3)	Middle (5) and inner (6)

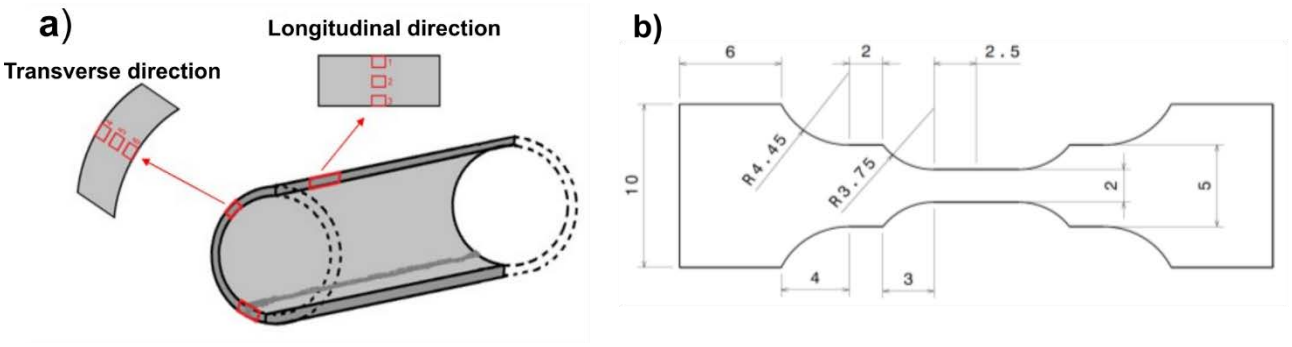

Figure 3: (a) Schematic illustration of pipeline with magnified view of possible positions for sample extraction, in both longitudinal and transversal direction and (b) specimen geometry for micromechanical tensile tests (units in mm).

2.3 Microstructural Characterization and Analysis

The microstructures of the materials were examined using both optical microscopy (OM) and scanning electron microscopy (SEM, Quanta FEG 650, FEI Inc.) equipped with a backscatter electron (BSE) detector and Everhart Thornley (ET) detector, that allows for electron backscatter diffraction (EBSD) analysis and electron channelling contrast imaging (ECCI). The microstructural characterization methods were performed on both Steel A and Steel B before and after testing.

EBSD measurements were acquired using an accelerating voltage of 20 keV, aperture size 3 (100 µm) and a step size of 0.2 µm. Diffraction patterns were collected with a Nordif camera, indexing and analysis were performed using the OIM software. Among multiple options from the OIM software, grain size, grain boundary misorientation and kernel average misorientation (KAM) have been of interest in the present work. The grain size can be determined for the various phases present in the material as well as the overall average grain size in the sample. Grain boundary misorientation describes the relationship between the crystallographic orientation of two neighbouring grains of the same phase. The KAM describes the average misorientation between any given point and its nearest neighbours in the same grain. To ensure no contribution from high angle boundaries, a misorientation threshold (typically <5°) is chosen and the average of all nearest neighbour angle values smaller than the threshold is computed [7]. The magnitude of KAM is

sensitive to scan step size and misorientation threshold. Higher values of KAM are related to higher densities of dislocations/plasticity in the material.

Electron channelling contrast imaging (ECCI) is another powerful SEM-based technique which, to some extent, is an alternative to TEM, as it requires less advanced sample preparation and bulk samples are used. Overall, it is a more time efficient method and can provide detailed information about the hydrogen influence on the plasticity behaviour by examining the dislocation structure and evolution at different strain levels. Since the presence of hydrogen has been proved to have a significant influence on the dislocation behaviour and thereby altering the material deformation , this technique is expected to provide a vital contribution to the assessment of hydrogen material interaction and damage mechanisms [8].

2.4 Nanoindentation

In order to determine the mechanical properties of the various microstructures in the pipeline steels, the nanoindentation technique was employed using a Hysitron Ti 950 TriboIndenter®, shown in Figure 4. The indenter system has a load resolution of <1 nN and displacement resolution of <0.02 nm [9]. Through quasistatic nanoindentation the equipment can be used to measure quantities such as hardness, fracture toughness, Young's modulus and friction coefficient. Information about the surface topography can be obtained using the scanning probe microscope (SPM) imaging option, where images are processed using the open-source software, Gwyddion. In the current work, each tested area had dimensions up to 60 µm x 60 µm with 10 x 10 indentations arrays. All tests were performed using a peak load of 1000 µN using the standard three-sided Berkovich tip, with a half angle of 65.35°. The distance between each indent was 4 µm, thus avoiding overlapping of the plasticity extension from each indent. The loading condition resulted in average maximum penetration depths ranging from 65 to 80 µm, depending on the hardness of the indented phase. A typical load vs. time plot is shown in Figure 5 and a schematic illustration of the in-situ hydrogen charging set up for nanoindentations, is shown in Figure 6.

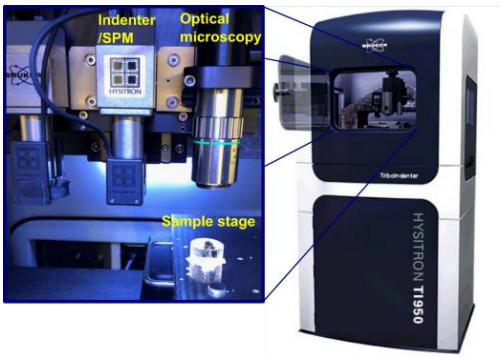

Figure 4: Hysitron Triboindenter Ti 950 [9]. The magnified view of the test chamber shows the indenter, optical microscopy and sample stage. Image taken from the instrument in Nanomechanical Lab (NTNU).

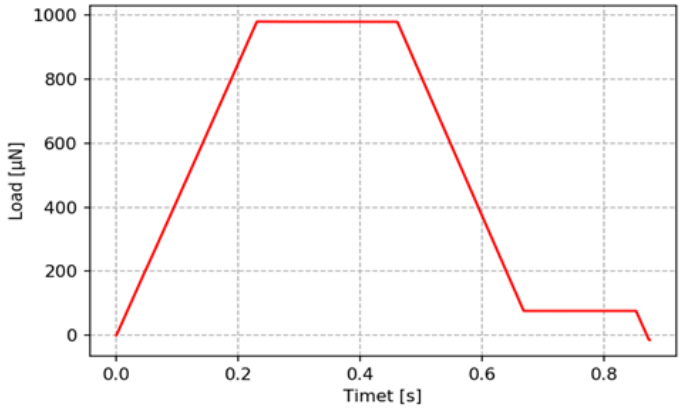

Figure 5: Load vs. time plots used for nanoindentation of (a) bainite and (b) ferrite in Steel A.

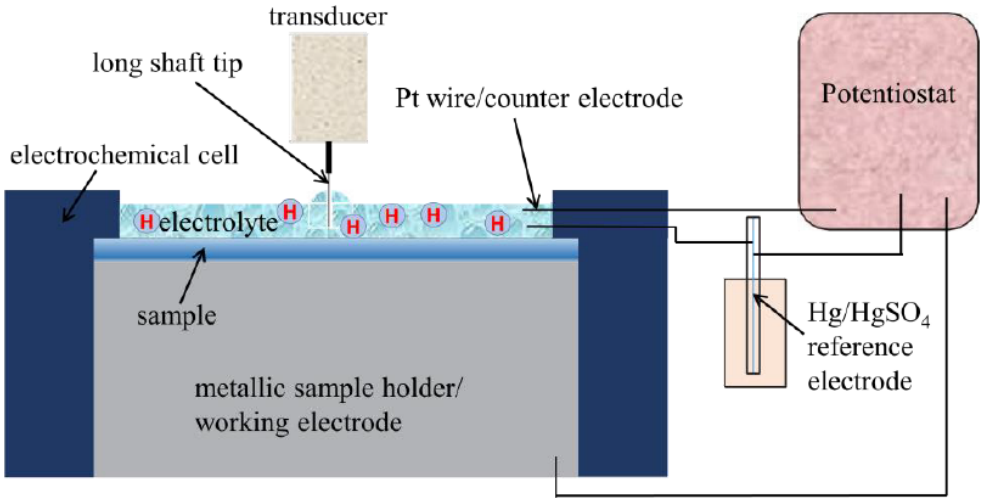

Figure 6: Schematic illustration of the in-situ hydrogen charging set up for nanoindentations.

The principles of nanoindentation as a test method are largely based on contact mechanics, the study of solid surface interaction [10]. Sharp tips are traditionally used for hardness measurements, such as Vickers (4-sided), cube corner (3-sided) and Berkovich (3-sided), whereas the Berkovich indenter is the most employed for nanoindentation hardness testing. It has the same projected area as the Vickers indenter (equivalent cone area function), shown in Figure 7 [11].

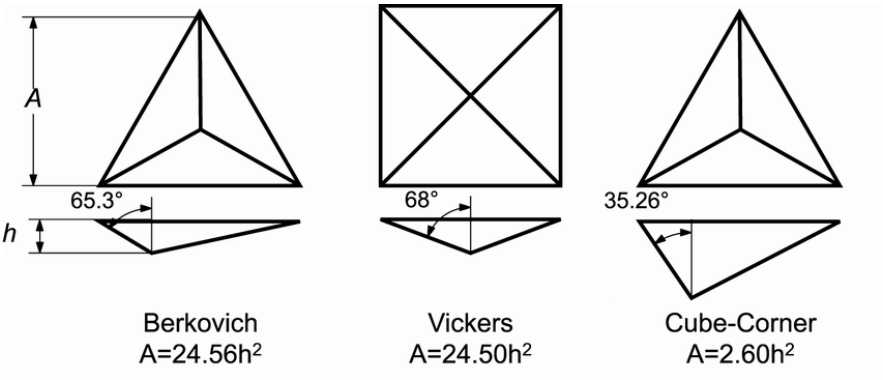

Figure 7: Most employed sharp indenter tips used for nanoindentation [11].

During nanoindentation the peak load, P_{max}, the corresponding contact depth, h_c and the slope of the unloading curve, S, are measured. The widely employed Oliver and Pharr [12] methodology reports that the hardness, H of a sample is determined by

$$H = \frac{P_{max}}{A(h_c)} \qquad \textbf{Eq. 2}$$

The unloading contact stiffness at maximum depth is given by:

$$S = \frac{dP}{dh} = \frac{2}{\sqrt{\pi}} E_r \sqrt{A} \qquad \textbf{Eq. 3}$$

where dP_{max}/dh is the initial slope of the unloading segment. For a perfect Berkovich indenter $A=24.56hc^2$. However, the projected contact area differs from this value as the tip is gradually worn out after use. Rearranging this formula provides an equation for the reduced modulus, E_r:

$$E_r = \frac{\sqrt{\pi}}{2} \frac{S}{\sqrt{A}} \qquad \textbf{Eq. 4}$$

The reduced modulus represents a combination of elastic stiffness of the sample and the tip. Modulus of elasticity E, of the sample is given by:

$$\frac{1}{E_r} = \frac{1 - v_{specimen}^2}{E_{specimen}} + \frac{1 - v_{indenter}^2}{E_{indenter}} \quad \textbf{Eq. 5}$$

where E_i *and* v_i are the Young's modulus and Poisson's ratio of the indenter tip and v is the Poisson's ratio of the sample [13].

The nanoindentation hardness differs from Vickers hardness calculations, also shown in Eq. 2, where the projected area of contact at the maximum load is used for calculation of hardness, whereas Vickers hardness is calculated after testing, measuring the residual imprint. Elastic relaxation can occur in some materials after testing. Certain errors may arise in the nanoindentation methods if pile-up occurs, the Oliver Pharr method may not yield accurate results [14, 15]. Thermal and/or electronic drifts and creep may also lead to erroneous results, but these can both be accounted for thus eliminating the source of error [14].

2.5 Electrochemical Charging

Samples cut from Steel A and Steel B were hydrogen pre-charged (for micromechanical tensile testing) and in-situ hydrogen charged (for nanoindentation), using electrochemical hydrogen charging for both 24 hours and 96 hours. The set-up for electrochemical hydrogen pre-charging before tensile tests, is shown in Figure 8. The set-up consists of the specimen (i) which acts as a working electrode and is being charged, an AgCl reference electrode (ii) and a platinum counter electrode (iii). The charging was conducted at both 65°C and at room temperature. After charging the specimen was washed by distilled water and ethanol before test was performed. The dwell times between end of charging and starting of tensile test were 12 minutes and 2 minutes, for tests performed in the SEM chamber (vacuum condition) and in air, respectively. One major challenge with pre-charging (for bcc materials) is the fast outgassing of hydrogen during the dwelling time as well as during testing, leaving specimens with low concentrations of hydrogen by the time a test is completed. Optimising the charging conditions by in-situ charging, to both simulate realistic subsea pipeline conditions and ensure minimal outgassing by the time of testing is important and is currently under development.

The electrolyte used was a glycerol-based solution consisting of 600 g of sodium tetraborate decahydrate (Borax) and 1 litre of glycerol. This mixture was then diluted with 20% distilled water before use. In-situ electrochemical small-scale testing can last for several hours (including both charging and testing) and it is important to ensure that the sample surface remains unchanged during charging. Many electrolytes may be too aggressive and can cause very localized corrosion on the sample surface. While the effect of such localized corrosion processes can be considered negligible when conducting macroscopic tests, this may very well not be the case for the high-resolution data from nano/micro-scale tests where unrealistically large effect may be observed. The glycerol-based electrolyte utilised in this study has a very low solubility and diffusivity of oxygen. This makes it appropriate for preserving the sample surface from corrosion throughout the entire testing procedure.

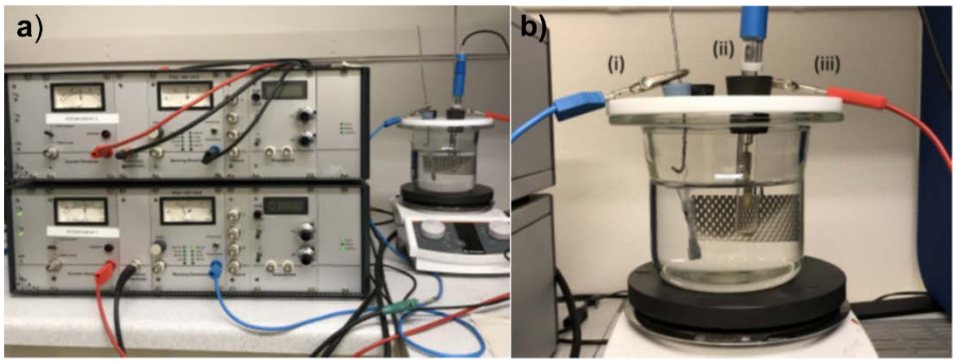

Figure 8: The electrochemical charging set-up used for hydrogen pre-charging. (a) Full set-up (b) close-up image of the electrodes in the electrolyte.

2.6 In-situ Micromechanical Tensile Tests

Micromechanical tensile tests were performed using a tensile/compression module from Kammrath & Weiss GmbH inside the SEM (Quanta FEG 650, FEI Inc), shown Figure 9. Specifications for the equipment are presented in Table 6. Pre-charged samples cut from Steel A and Steel B, were tested in transversal and longitudinal direction, from the inner and middle position of the pipe, as illustrated in Figure 3. Tensile samples were charged for 24 and 96 hours before being tested inside SEM in vacuum and in air with a displacement rate of 2.5 µm/s. While testing in air outside the SEM chamber does not allow for high-resolution imaging during testing, it permits a significant reduction of the dwell time and consequently greatly limiting outgassing of hydrogen before testing. Table 7 shows the test parameters used in this work.

Table 6: Equipment specifications of the Kammrath \& Weiss GmbH tensile/compression module.

Load range	10µN – 5 kN
Sample maximum size [mm]	60 x 10 x 5
Displacement speed range [µm/sec]	0.1. - 20
Total displacement [mm]	45
Displacement resolution [nm]	100
Load cell range	10N – 10 kN

Table 7: Test specifications and parameters for tensile tests of Steel A and Steel B.

Charge time	Pre-charged 24h	Pre-charged 96h	No charging (Ref.)
Temperature	65 °C	65 °C	65 °C and RT
Strain rate	5×10^{-4}	5×10^{-4}	5×10^{-4}
Test Environment	Vacuum and air	Vacuum and air	Vacuum and air

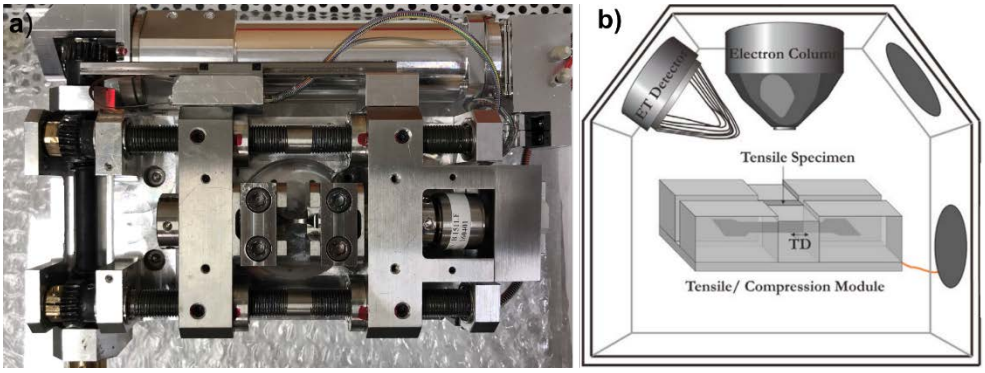

Figure 9: a) In-situ tensile testing device from Kammrath Weiss with sample mounted in the centre of the equipment and b) schematic illustration of the tensile/compression device mounted inside the SEM chamber (Figure 9b) adapted from [16]).

3 Results

3.1 Characterization of Microstructure

Figure 10 shows SEM micrographs of Steel A, consisting of ferrite and bainite indicated with F and B, respectively. The EBSD analysis of Steel A are shown in Figure 11 (a-c). The as-received microstructure is shown in an a) image quality (IQ) map and a b) crystal orientation map, displayed in inverse pole figure (IPF) colouring, which reflects the local detected orientation. The pole figure inset in the IPF image, represents the specific sample direction within the crystal system. Figure 11 c) shows the KAM image, where misorientations between the centre point of the kernel and all surrounding points in the kernel are calculated and averaged, resulting in the local misorientation of the centre point. The results reveal higher misorientation/KAM values in the bainitic phase, indicating a higher density of distortion, deformation and dislocations. Additionally, the low (2°-15°) and high angle (15°-65°) boundaries are marked as black and red, respectively. The majority of the grain boundaries are high-angle boundaries, covering 64.6 % of grain boundaries in this area and 35.4 % are low angle boundaries. The high-angle boundaries possess a higher free energy due to the distortion in the atom arrangement and the non-equilibrium state in the atom spacing. The average grain size of Steel A was found to be 7.1 µm for this scanned area. The EBSD scan is performed in the middle area of the pipewall

thickness and larger variations in grain size might be expected towards the inner area of the pipewall, that contain more bainite, as shown in the optical micrographs in Figure 1 c).

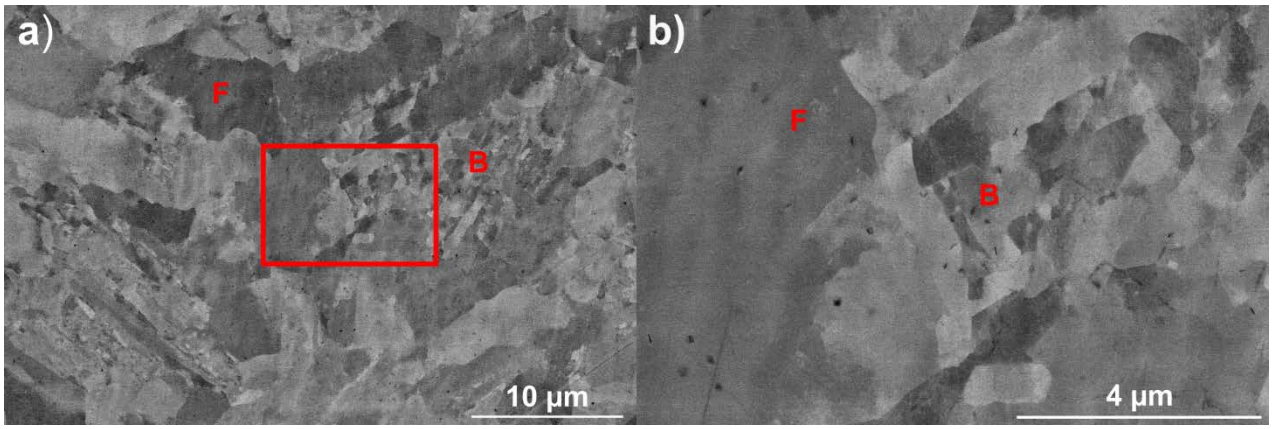

Figure 10: SEM micrographs in BSE-mode of Steel A X65 pipeline steel with ferrite and bainite indicated with F and B, respectively. The high-magnification image in b) is from the square inset in a).

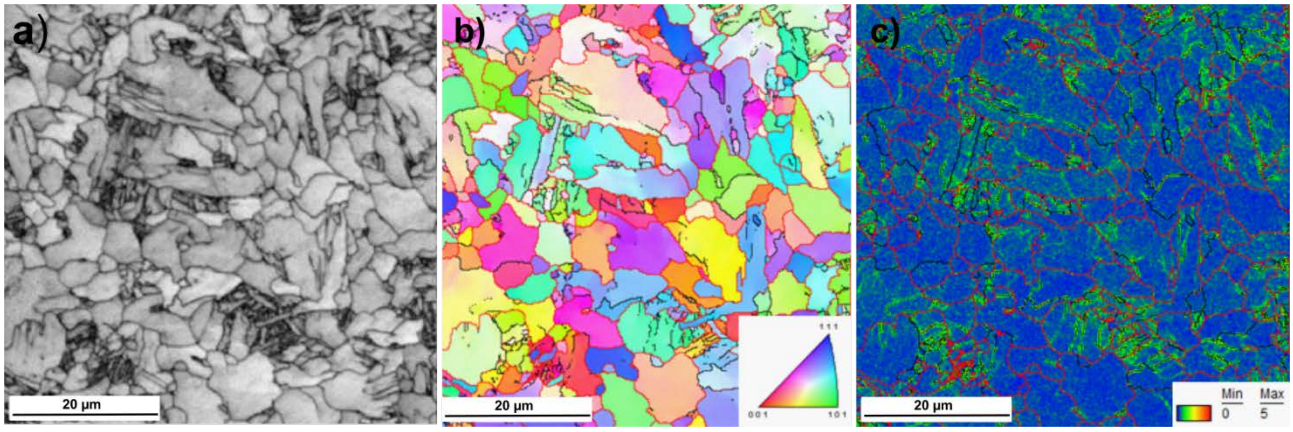

Figure 11: EBSD analysis of Steel A showing the a) as-received microstructure consisting of ferrite (light grey) and bainite (dark plates), b) IPF image, colour coded according to the crystallographic orientation and c) KAM image with high-angle (red) and low angle (black) grain boundaries marked.

Electron channelling contrast imaging (ECCI) was conducted for both steels before deformation. As shown in Figure 12 and Figure 13, the technique allows for visualization of nanometer-scale heterogeneities such as dislocations and interphases by using optimal sample surface orientations. However, it can also be advantageous for analysing more severe plasticity-related phenomenon in larger bulk samples.

ECC imaging of Steel A, reveals pre-existing defects in ferrite and bainite, shown Figure 12 a) and b), respectively. The dislocations observed in the ferrite (Figure 12) appear to be more homogeneously distributed than that observed in the bainitic phase (Figure 12 b). Moreover, from a qualitative point of view, the dislocation segments seem to be, in average, longer in the ferrite compared to those observed in the bainite, where the segments appear more localized, probably piled-up and interrupted by the discontinuities

in the bainitic microstructure. The results agree with the EBSD KAM analysis presented in Figure 11b) revealing higher distortion in the bainite.

Steel B consist of ferrite and pearlite that are depicted in Figure 13 a-b). Overall, limited pre-existing defects are observed here, except for a few dislocation lines close to interphases and in between the cementite lamellas in Figure 13 a).

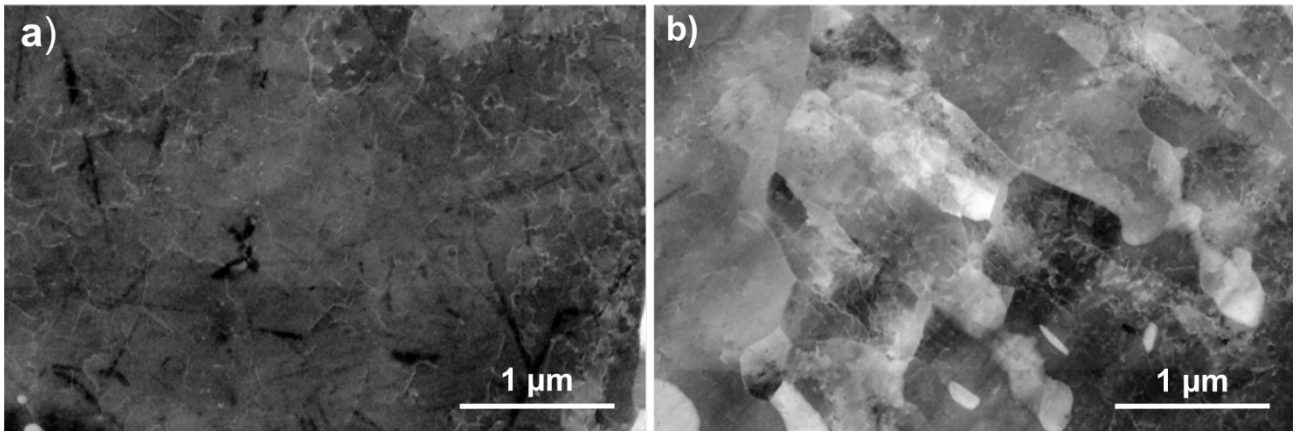

Figure 12: Electron channelling contrast imaging of Steel A pipeline steel in the a) ferrite and b) bainite phase revealing dislocation distribution and microstructural defects at nano-micrometer scale.

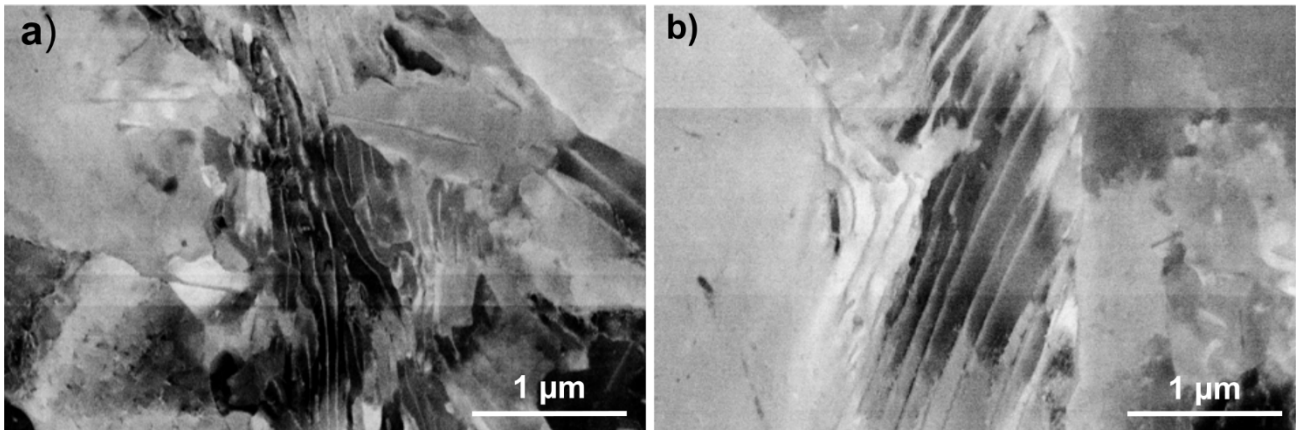

Figure 13: Electron channelling contrast imaging of Steel B pipeline steel revealing the cementite lamella in the pearlite phase from two different regions a) and b).

3.2 Micromechanical Tensile Testing

In-situ micromechanical tensile tests were performed on specimens cut from Steel A and Steel B in longitudinal and transverse direction, from the middle and inner position of the pipe, as illustrated in Figure 3. Testing was conducted under four different conditions: In vacuum without hydrogen pre-charging, 24 hours pre-charging, 96 hours pre-charging and in air for comparison. Hydrogen charging was performed using a glycerol-based electrolyte with extremely low solubility and diffusivity and it is used due to its corrosion-free properties, as described in section *2.5. Electrochemical Charging.*

Figure 14 shows the nominal stress-strain curves from the tensile testing of Steel A and B. Overall, both materials undergo some hydrogen-induced degradation in terms of reduced strength and elongation, as shown in Table 8. However, the influence of hydrogen pre-charging, is not that prominent in the current results. For instance, Steel A-Inner position is barely affected after 96 hours pre-charging. It is speculated that the small effect of hydrogen on the tensile properties could be due to the high temperature during pre-charging (65 °C) and/or long dwell time between charging and testing of the specimens in the vacuum chamber. This, in combination with the fast diffusion and outgassing of hydrogen typical of BCC structures in the pipeline steels would determine a relatively low hydrogen concentration in the sample during testing. In order to verify the assumptions, additional tests were performed in order to trace the aforementioned parameters. Firstly, the pre-charging temperature was changed from 65 °C to room temperature, and subsequently tested in the SEM. However, no prominent detrimental effect from hydrogen occurred. Finally, additional tests of Steel A transversal direction (inner position) were charged for 24 hours and performed in air atmosphere instead of vacuum condition in SEM. This reduced the dwell time from 12 to 2 minutes. As shown in Figure 15, a clear hydrogen detrimental effect can be observed an quantified with a 16.7 % reduction of elongation to fracture. The result from the tensile test in air confirms that the fast hydrogen outgassing in BCC structure is a significant challenge for hydrogen studies performed on pre-charged specimens, hence the dwell time should be as short as possible or preferentially, experiments should be performed with in-situ hydrogen charging.

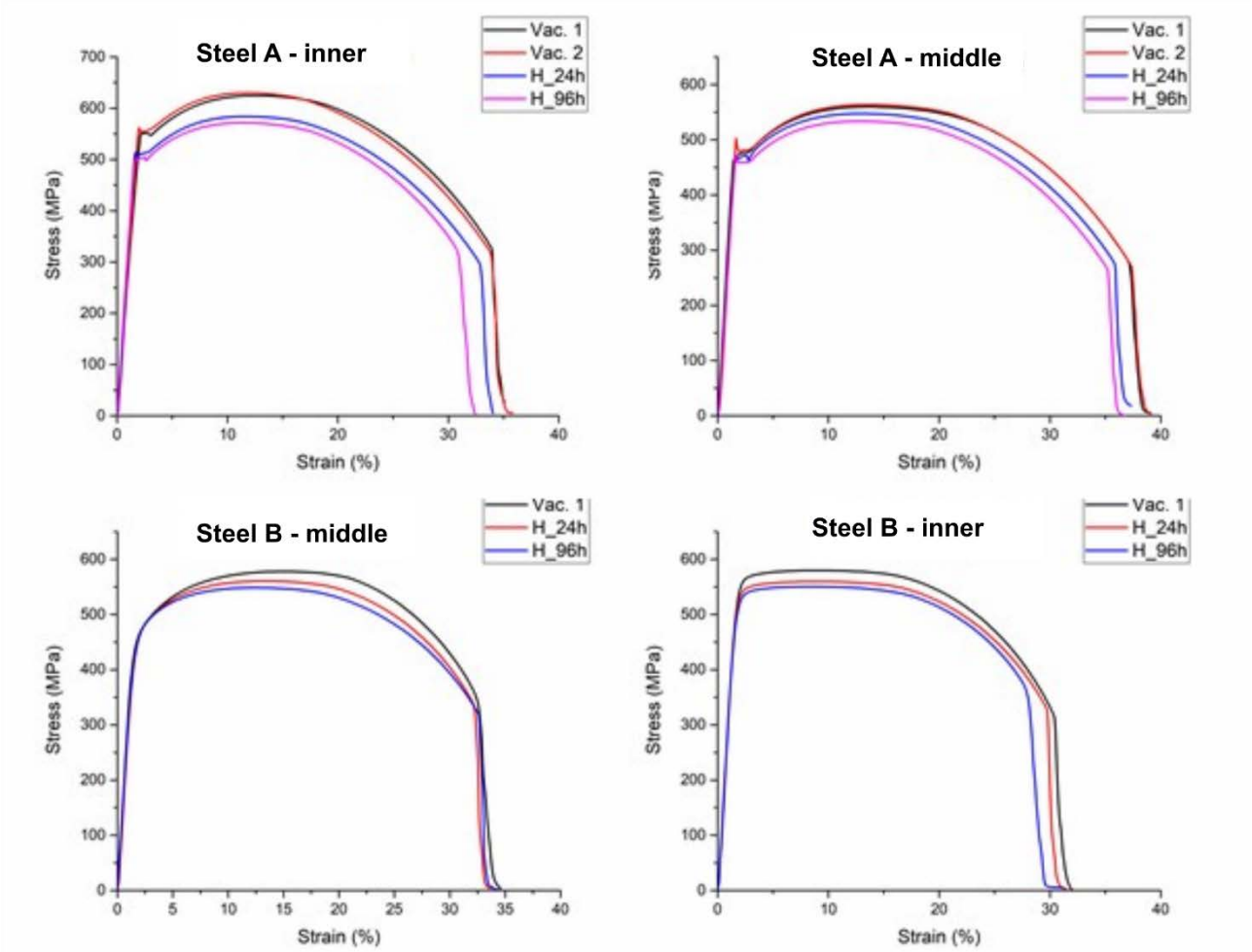

Figure 14: Nominal stress-strain curves from in-situ micromechanical tensile test of X65 pipeline steels (Steel A and Steel B) in longitudinal direction, from both inner and middle position of the pipewall thickness. Black and red curves are from uncharged samples and blue and pink curves are from hydrogen pre-charged sample in 24 hours and 96 hours, respectively.

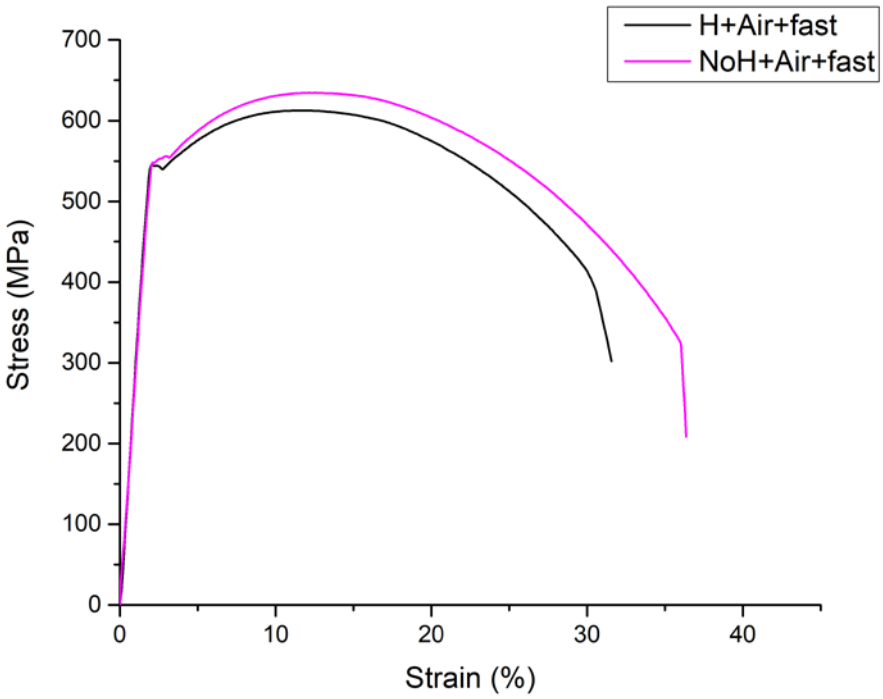

Figure 15: Nominal stress-strain curves from micromechanical tensile tests of Steel A transversal direction from the inner position of the pipewall thickness after 24 hours pre-charging at room temperature.

Table 8: Tensile properties from samples cut from inner and middle position of Steel A and Steel B, X65 pipeline steels, in longitudinal and transverse direction. Tests are performed in air and vacuum after hydrogen pre-charging (and without charging for comparison).

Steel	Test Environment	Strain rate [s^{-1}]*	Temp [°C]	σ_y [MPa]	σ_{UTS} [MPa]	El
X65 Steel A (L) Middle	Vacuum	5×10^{-4}	RT	480.4	559.7	
	24 h pre-charged			463.4	543.1	2.86%
	96 h pre-charged			459.9	534.3	4.69%
X65 Steel A (L) Inner	Vacuum	5×10^{-4}	RT	546.0	622.2	
	24 h pre-charged			509.6	580.5	0.86%
	96 h pre-charged			502.1	571.7	6.29%
X65 Steel A (T) Middle	Vacuum	5×10^{-4}	RT	508.4	597.6	
	24 h pre-charged			509.9	584.7	5.71%
	96 h pre-charged			501.0	574.5	7.44%
X65 Steel A (T) Inner	Vacuum	5×10^{-4}	RT	564.9	642.1	
	24 h pre-charged			554.7	627.2	3.07%
	96 h pre-charged			545.3	618.0	6.42%
X65 Steel B (L) Middle	Vacuum	5×10^{-4}	RT	462.2	572.2	
	24 h pre-charged			458.75	560.6	1.46%
	96 h pre-charged			459.2	545.2	1.75%
X65 Steel B (L) Inner	Vacuum	5×10^{-4}	RT	553.9	577.0	
	24 h pre-charged			538.3	555.7	0.22%
	96 h pre-charged			523.2	542.8	3.81%
X65 Steel B (T) Middle	Vacuum	5×10^{-4}	RT	500.3	581.5	
	24 h pre-charged			492.3	577.9	2.59%
	96 h pre-charged			485.7	571.7	4.92%
X65 Steel B (T) Inner	Vacuum	5×10^{-4}	RT	508.2	576.1	
	24 h pre-charged			502.4	573.7	9.02%
	96 h pre-charged			500.1	566.9	8.53%

L= Longitudinal oriented sample

T= Transverse oriented sample

***Calculated based on displacement rate and specimen dimension**

3.3 Fractography

Figure 16 shows the post-mortem fractography characterization on Steel A specimens with and without hydrogen exposure. Specimens cut from the inner and middle position of the pipewall thickness are shown in Figure 16 (a-b) and (c-d), respectively. Fractography revealed the expected ductile microvoid coalescence

(MVC)-assisted failure in the uncharged samples and limited evidence of HE in hydrogen pre-charged samples, also indicated in the obtained nominal stress-strain data, as shown in Figure 14. However, the fracture surface contains some features indicating influence of the hydrogen charging. For instance, larger voids occur in pre-charged specimens, indicated with the dotted circles in Figure 16. It is speculated that, due to quick outgassing, the only hydrogen left in the material during testing is the one in the traps. The observed larger voids could be related to heterogeneities where hydrogen is strongly trapped (high binding energy), resulting in local embrittling. Steel B display comparable fractography features as those observed in steel A; for both test conditions the fracture surface solely revealed dimpled morphologies inherent to MVC mechanisms, with the presence of a few larger voids on specimens tested after pre-charging, as shown in Figure 17.

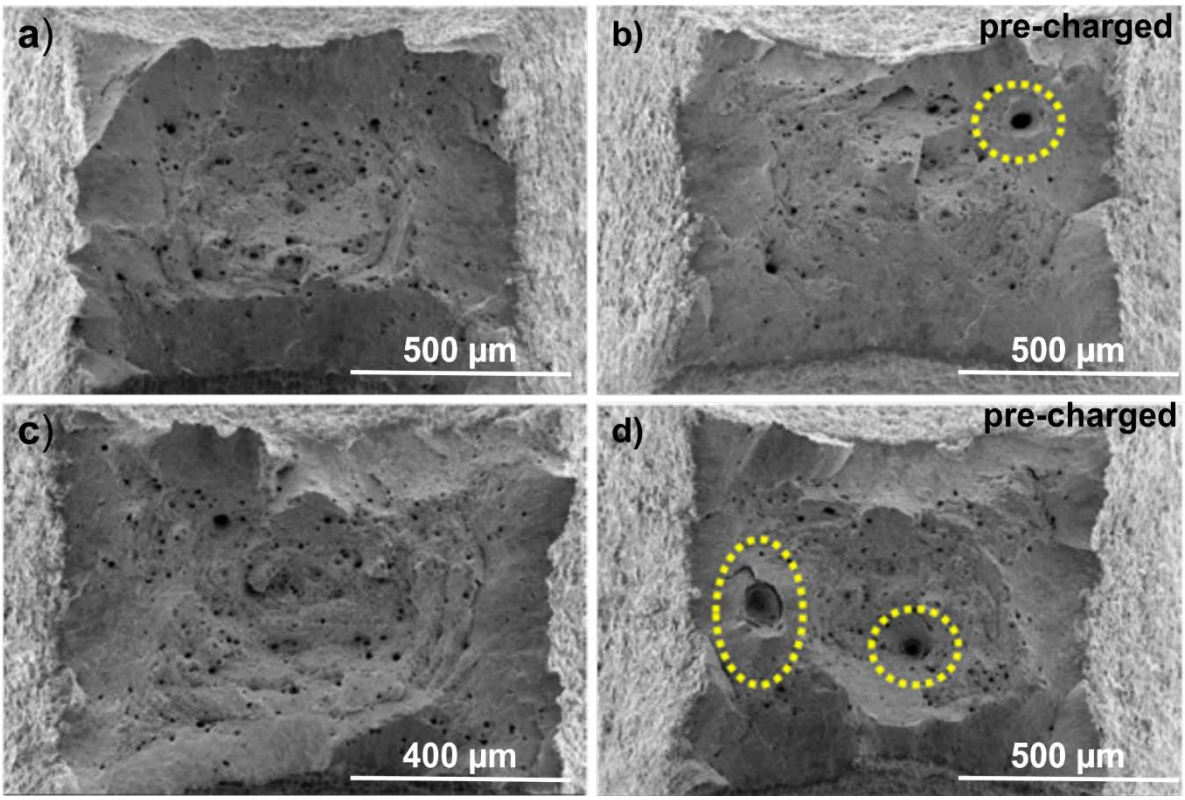

Figure 16: Fractography of Steel A in the a-b) inner and c-d) middle area of pipewall from tests in a) and c) vacuum without pre-charging and after b) and d) 96 hours hydrogen pre-charging.

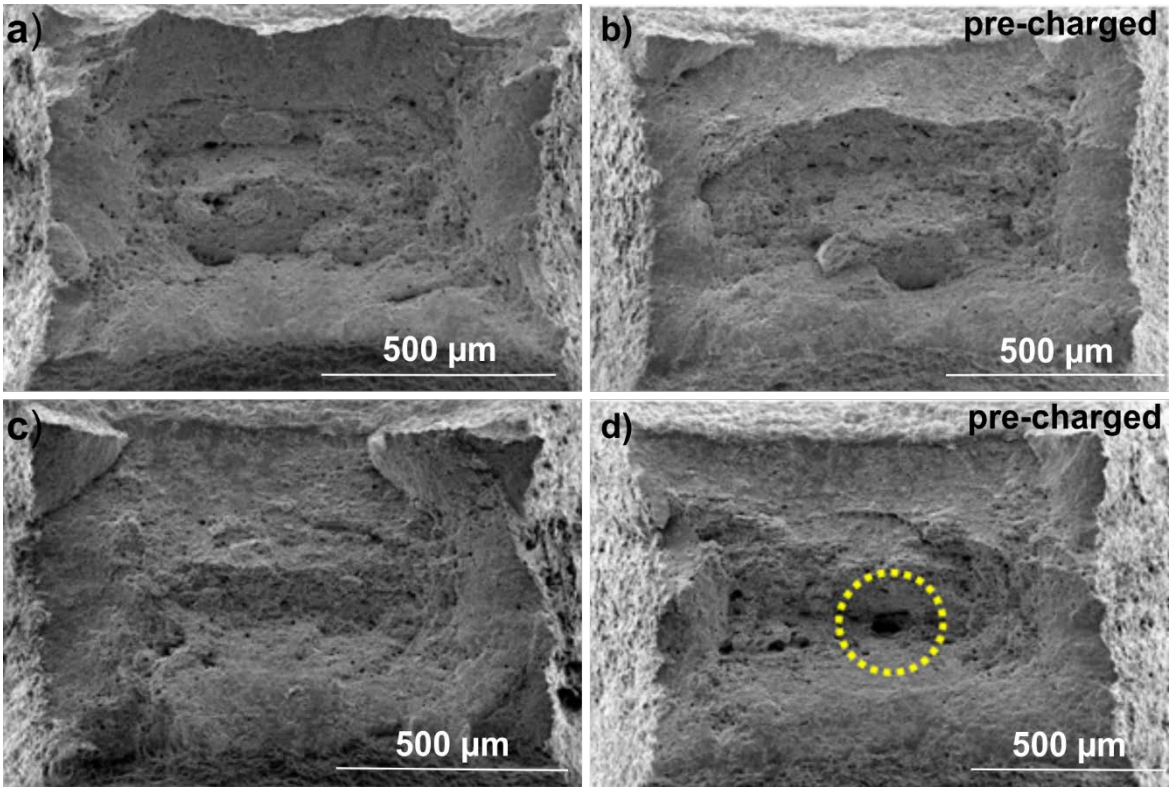

Figure 17: Fractography of Steel B in the a-b) inner and c-d) middle area of pipewall from tests in a) and c) vacuum without pre-charging and after b) and d) 96 hours hydrogen pre-charging.

3.4 Nanomechanical properties

Nanoindentations tests were conducted in air and under in-situ electrochemical charging conditions. Typical load-displacement curves obtained after tests in air and in hydrogen environment for the Steel A, are shown in Figure 18. The red and black curves represent ferrite and bainite, respectively. The load-displacement curves consist of four distinct stages: (1) Initial elastic loading; (2) pop-in, attributed to the onset of plastic deformation and the first dislocation nucleation [17]; (3) elasto-plastic deformation and finally (4) elastic unloading. As shown in Figure 18, all loading stages, except for the initial elastic loading, display differences depending on the indented microstructure and test environment. The main alternations seen from hydrogen charging conditions, are reduced pop-in load and increased nanohardness.

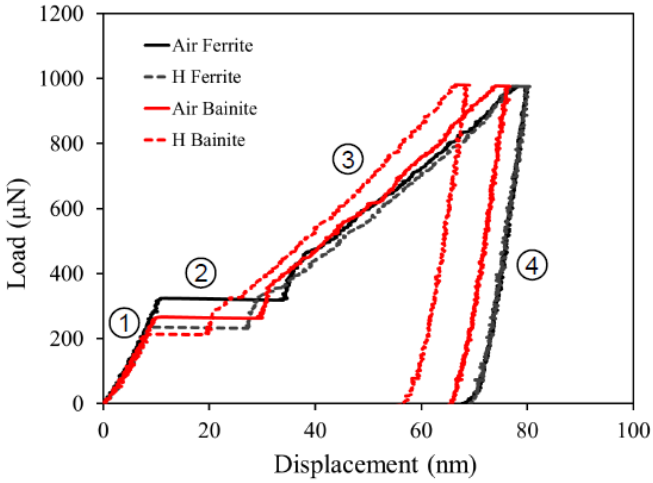

Figure 18: Load-displacement curves from nanoindentations in ferrite (black curves) and bainite (red curves) in Steel A under in-situ electrochemical charging (dotted curve) and in air (line curve).

Figure 19 a) and b), shows the average hardness and pop-in load obtained from nanoindentation tests in Steel A. Overall, it is observed an increased hardness and reduced pop-in load for tests performed in electrochemical charging conditions. The alternation in hardness is more obvious for the bainitic phase, with an increase of 11 % compared to 2.6 % for ferrite. The first pop-ins are initiated at different load levels, depending on environment and indented phase, as shown in Figure 19 b). From tests in air, the pop-in load for bainite is lower than ferrite and a subsequent reduction of 25.7 % and 14.9 % occurs when testing under electrochemical hydrogen charging conditions, for ferrite and bainite, respectively. Figure 20 a) and b) reveal comparable behaviour for the steel B, i.e., an increase in hardness and a reduction in pop-in load under in-situ electrochemical charging conditions. Also, here, a more prominent hardness increment is obtained for pearlite/bainite, compared to that for ferrite, i.e., 12.4 % vs. 4.21 %.

Analysis of the current results is part of ongoing work, but results obtained from in-situ electrochemical nanoindentation are in accordance with previous reported observations. The increment in nanohardness obtained in hydrogen environment have been attributed to the hydrogen-enhanced effect on lattice friction and hydrogen-reduced plastic zone size [18]. As shown from ECCI in Figure 12, the as-received Steel A contains pre-existing dislocations in the material (bright features). These are, qualitatively, more prominent in bainite (Figure 12b)), compared to that observed in ferrite (Figure 12a)), thus probably introducing a higher enhanced lattice friction during in-situ electrochemical hydrogen charging. The reduction in pop-in load obtained in the electrochemical condition, has been explained by the Defactant model [19], proposing that hydrogen can reduce the formation energy of defects, and enhance the defect formation. As seen from our results, less load is required to initiate the first dislocation nucleation when hydrogen is present.

In general, we distinguish between two types of dislocation nucleation: homogeneous and heterogeneous dislocation nucleation [20]. It is suggested that homogeneous dislocation nucleation is associated to the first pop-in during nanoindentation [21], involving the processes of atomic motion to form a dislocation loop close to the theoretical values of shear strength. This means that homogeneous dislocation nucleation occurs in a defect free zone. However, it has been indicated that the presence of pre-existing defects such as vacancies, vacancy clusters, dislocations and impurities could result in heterogeneous dislocation nucleation [22]. In this

case, the pre-existing dislocation is nucleated instead of nucleating a new dislocation as they usually require lower activating force than homogeneous dislocation nucleation. It is possible that such mechanisms, i.e., heterogeneous dislocation nucleation rather than new dislocation nucleation, can explain the lower obtained pop-in loads for bainite and pearlite, where higher number of pre-existing defects than ferrite may be expected. Post-morten SEM characterization were performed after indentation to confirm the indented microstructure and exclude data from indentation interfering with grain and/or phase boundaries, shown in Figure 22 and Figure 23 for Steel A and Steel B, respectively.

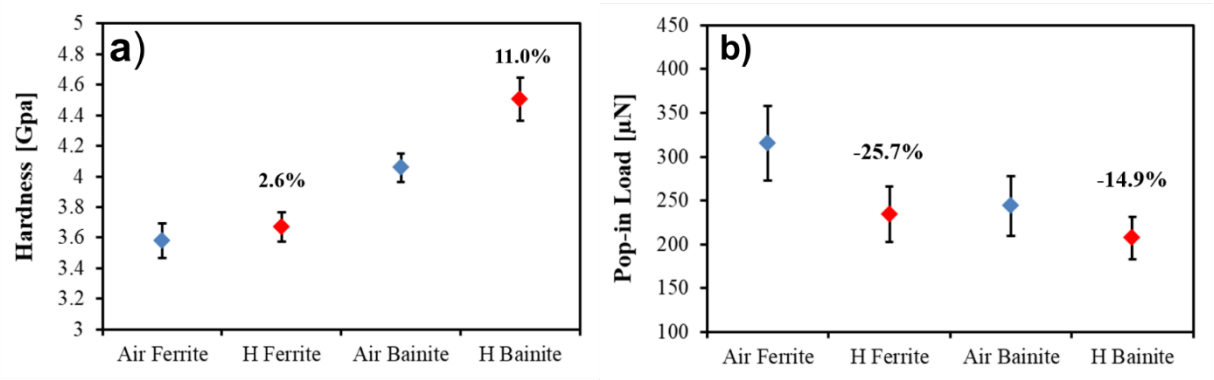

Figure 19: Average a) hardness values and b) pop-in load with standard deviation, for ferrite and bainite tested in air and under in-situ electrochemical hydrogen charging.

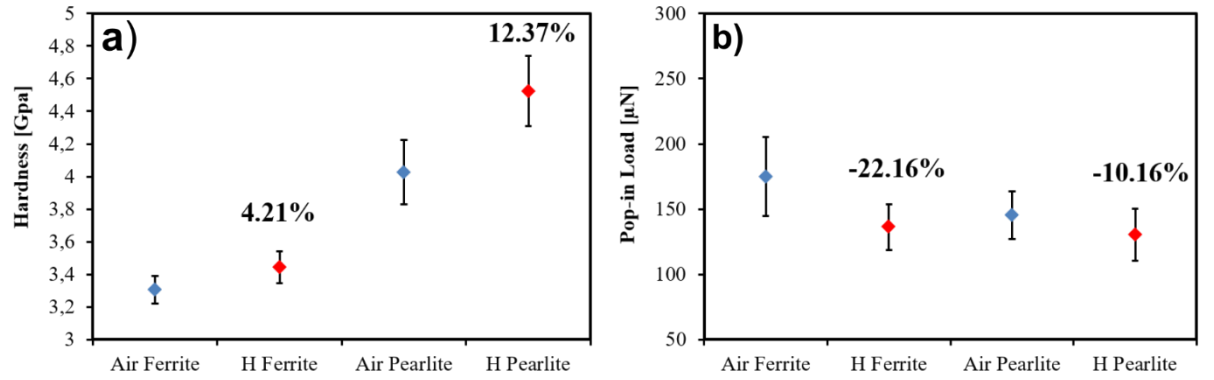

Figure 20: Average a) hardness values and b) pop-in load with standard deviation, for ferrite and pearlite tested in air and under in-situ electrochemical hydrogen charging.

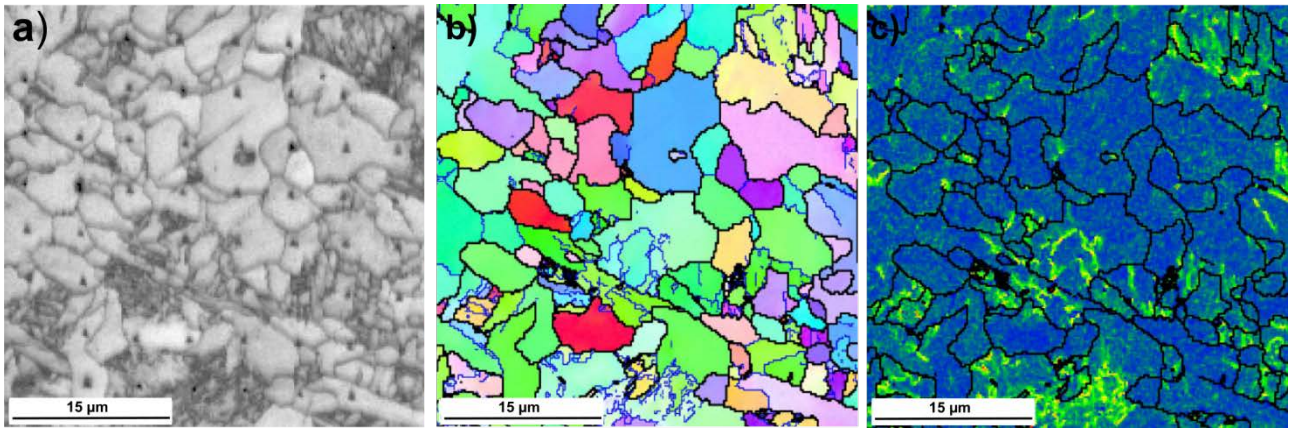

Figure 21: Post-mortem SEM imaging on sample surface after in-situ electrochemical nanoindentation on Steel A.

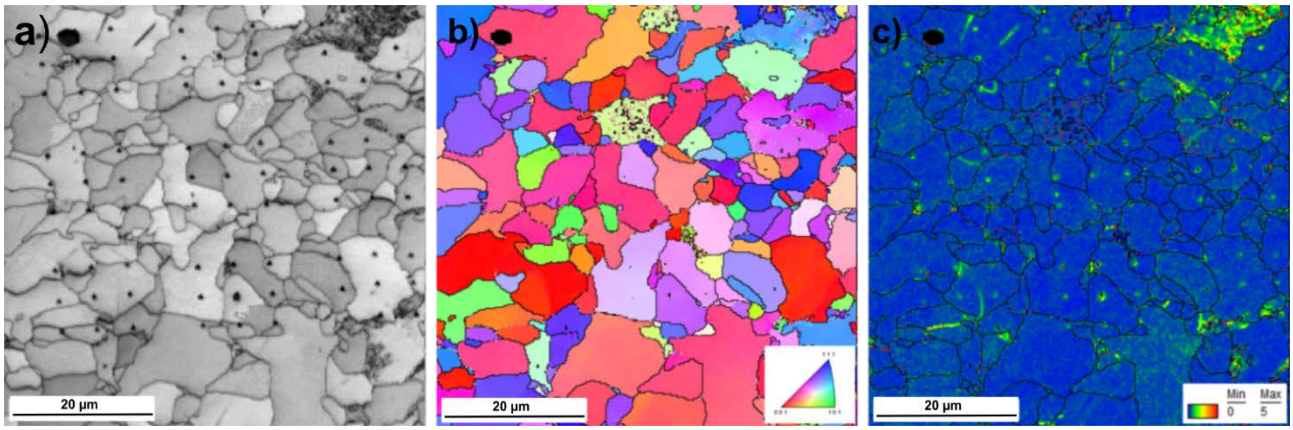

Figure 22: Post-mortem SEM imaging on sample surface after in-situ electrochemical nanoindentation on Steel B.

Electron channelling contrast imaging (ECCI) have been conducted to investigate the dislocation sub-structure close to the residual nanoindentation imprints to elucidate differences in plasticity evolution after testing in air and under electrochemical hydrogen charging. Currently, results exist for Steel A, shown in Figure 23. The nanoindentations performed in air reveal multiple dislocations along the indentation imprint sides shown as bright features in Figure 23 a-b). The extent of the plasticity is also evident from the brighter area around the imprint, indicated in the stippled line in Figure 23 a).

The characteristics observed after tests in electrochemical solution, obtain a different character, as shown in Figure 23 c-d). The dislocation activity appears to be affected by the presence of hydrogen seen from the different characteristics of plasticity close to the indents, for the two test environments. Dislocation activity from tests in air appear to be more prominent seen from the extend of the plasticity zone around the residual nanoindentation imprint and dislocations Figure 23 a-b). Whereas plasticity is less evident in the hydrogen case, Figure 23 c-d). Moreover, the residual area radius indicates a harder bainitic phase and a hydrogen enhanced hardness, consistent with the obtained hardness data shown in Figure 19.

The hydrogen effect on dislocation activity has previously been investigated using in-situ TEM, nanoindentation and microcantilever bending tests in both gaseous and electrochemical hydrogen environment. Hydrogen is shown to facilitate dislocation nucleation, enhance slip localization and reduce dislocation mobility [23-27]. Cross slip and climbing mechanisms are less pronounced in the presence of hydrogen which inhibit the dislocation cell formation below the indenter [27]. The current findings in this work are consistent with previously reported findings related to hydrogen influence on plasticity. Due to technical problem and delays related to COVID restrictions, ECCI analysis of Steel B could not be realized so far and and will be a part of future journal paper from this work.

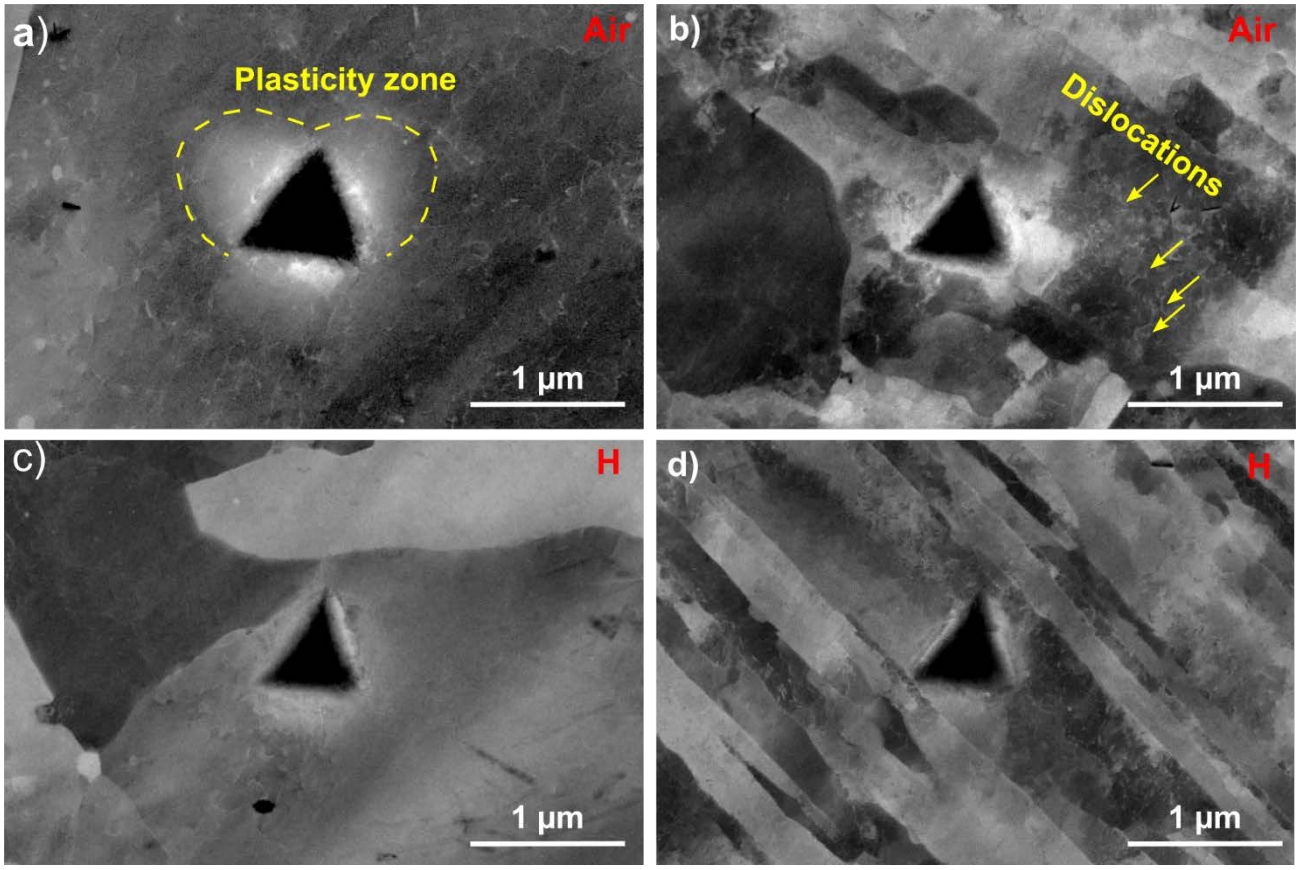

Figure 23: Electron channelling contrast images of residual nanoindentation imprints after tests in a-b) air and in c-d) electrochemical solution in Steel A.

4. Summarizing Remarks

In-situ nano and micromechanical testing combined with SEM-based characterization techniques were used to study both the global and localized effect of hydrogen in mechanical conditions for a new (Steel A) and a vintage (Steel B) X65 pipeline steel. From the current work, the main findings are summarized as follows:

- In-situ micromechanical tensile tests of pre-charged specimens provide insight into the deformation evolution and the hydrogen influence of the microstructural features. However, results show that hydrogen pre-charging of bcc ferritic pipeline steels is not optimum to capture the hydrogen effect on the mechanical properties due to the fast outgassing of hydrogen. A modified setup for in-situ charging is under development and will be used for the future publication on this work.
- The fractography of micro sized tensile specimens for both steels revealed dimpled morphologies, indicating ductile behaviour. However, a few larger voids were observed, possibly be related to heterogeneities acting as strong trapping sites for hydrogen, resulting in local embrittling.
- In-situ electrochemical nanoindentation reveal different behaviours between the present microstructures in Steel A and B, in air and hydrogen environment. The obvious drop in pop-in loads and increased nanohardness values observed when testing in hydrogen environment is obtained for all microstructures and attributed to the reduction of dislocation line energy and hydrogen-enhanced lattice friction, respectively. The pop-in load is higher for ferrite compared to the other microstructures, i.e., bainite and pearlite that contain more discontinuities and have higher initial dislocation densities, attributed to homogeneous and heterogeneous dislocation nucleation, respectively.

4 References

1. Bhadeshia, H.K.D.H., *Bainite in steel. Theory and practice.* . 3rd edition ed. 2015, United Kingdom: Maney Publishing on behalf of the Institute of Materials, Minerals & Mining.
2. Ashby, M.F.a.J., D.R.H, *Engineering Materials 2. An Introduction to Microstruc- tures, Processing and Design.* International Series on Material Science and Technology. 1988, Great Britain: Pergamon Press.
3. Antonio Alvaro, et al., *HyLINE Materials Screening: Slow strain rate tensile testing results*. 2020: SINTEF Industri. p. 62.
4. Joo, M.S., D.W. Suh, and H.K.D.H. Bhadeshia, *Mechanical anisotropy in steels for pipelines.* ISIJ international, 2013. **53**(8): p. 1305-1314.
5. Kec, J., et al., *Investigation of mechanical properties and microstructure of X60 line-pipe steel.* Procedia Structural Integrity, 2019. **17**: p. 230-237.
6. Feng, R., et al., *The Influence of Abnormal Segregation Band on Mechanical Properties of Hot Rolled Ferrite/Pearlite Steel Plate.* Materials Sciences and Applications, 2018. **9**(01): p. 81.
7. Badji, R., T. Chauveau, and B. Bacroix, *Texture, misorientation and mechanical anisotropy in a deformed dual phase stainless steel weld joint.* Materials Science and Engineering: A, 2013. **575**: p. 94-103.
8. Alvaro, A., et al., *Hydrogen enhanced fatigue crack growth rates in a ferritic Fe-3 wt%Si alloy and a X70 pipeline steel.* Engineering Fracture Mechanics, 2019: p. 106641.
9. HYSITRON. *TI 950 TriboIndenter (R).* Available from: http://novaanalitik.com/pdf/hysitron-950.pdf.
10. Jackson, R.L., et al., *Contact Mechanics*, in *Tribology for Scientists and Engineers: From Basics to Advanced Concepts*, P.L. Menezes, et al., Editors. 2013, Springer New York: New York, NY. p. 93-140.
11. Jiménez-Piqué, E. and Y. Gaillard, *Instrumented Indentation of Layered Ceramic Materials.* Key Engineering Materials - KEY ENG MAT, 2007. **333**: p. 107-116.
12. Oliver, W.C. and G.M. Pharr, *Measurement of hardness and elastic modulus by instrumented indentation: Advances in understanding and refinements to methodology.* Journal of Materials Research, 2004. **19**(01): p. 3-20.
13. Oliver, W.C. and G.M. Pharr, *An improved technique for determining hardness and elastic modulus using load and displacement sensing indentation experiments.* Journal of materials research, 1992. **7**(6): p. 1564-1583.
14. Smallman, R. and A. Ngan, *Modern Physical Metallurgy (Eight Edition).* Chapter, 2014. **5**: p. 219.
15. Goto, K., I. Watanabe, and T. Ohmura, *Inverse estimation approach for elastoplastic properties using the load-displacement curve and pile-up topography of a single Berkovich indentation.* Materials & Design, 2020. **194**: p. 108925.
16. Wan, D., Y. Deng, and A. Barnoush, *Hydrogen embrittlement effect observed by in-situ hydrogen plasma charging on a ferritic alloy.* Scripta Materialia, 2018. **151**: p. 24-27.
17. Barnoush, A., M. Asgari, and R. Johnsen, *Resolving the hydrogen effect on dislocation nucleation and mobility by electrochemical nanoindentation.* Scripta Materialia, 2012. **66**(6): p. 414-417.

18. Wang, D., et al., *Effect of hydrogen on nanomechanical properties in Fe-22Mn-0.6C TWIP steel revealed by in-situ electrochemical nanoindentation.* Acta Materialia, 2019. **166**: p. 618-629.

19. Kirchheim, R., *Revisiting hydrogen embrittlement models and hydrogen-induced homogeneous nucleation of dislocations.* Scripta materialia, 2010. **62**(2): p. 67-70.

20. Zhao, Y., et al., *Bimodality of incipient plastic strength in face-centered cubic high-entropy alloys.* Acta Materialia, 2021. **202**: p. 124-134.

21. Bei, H., et al., *Strength differences arising from homogeneous versus heterogeneous dislocation nucleation.* Physical Review B, 2008. **77**(6): p. 060103.

22. Zhu, C., Z.P. Lu, and T.G. Nieh, *Incipient plasticity and dislocation nucleation of FeCoCrNiMn high-entropy alloy.* Acta Materialia, 2013. **61**(8): p. 2993-3001.

23. Deng, Y. and A. Barnoush, *Hydrogen embrittlement revealed via novel in situ fracture experiments using notched micro-cantilever specimens.* Acta Materialia, 2018. **142**: p. 236-247.

24. Ferreira, P.J., I.M. Robertson, and H.K. Birnbaum, *Hydrogen effects on the character of dislocations in high-purity aluminum.* Acta Materialia, 1999. **47**(10): p. 2991-2998.

25. Nibur, K.A., D.F. Bahr, and B.P. Somerday, *Hydrogen effects on dislocation activity in austenitic stainless steel.* Acta Materialia, 2006. **54**(10): p. 2677-2684.

26. Deng, Y., et al., *In-situ micro-cantilever bending test in environmental scanning electron microscope: Real time observation of hydrogen enhanced cracking.* Scripta Materialia, 2017. **127**: p. 19-23.

27. Gong, P., et al., *Hydrogen suppression of dislocation cell formation in micro and nano indentation of pure iron single crystals.* Scripta Materialia, 2021. **194**: p. 113683.

Technology for a better society

www.sintef.no